Fatigue Failures at Defective Grains in a Single Crystal Nickel-Base Superalloy

T.P. Gabb, T.M. Smith, J.A. Nesbitt, J. Telesman, and C.A. Kantzos
Glenn Research Center, Cleveland, Ohio

I.E. Locci
University of Toledo, Toledo, Ohio

L.J. Evans and L.J. Ghosn
Glenn Research Center, Cleveland, Ohio

NASA STI Program . . . in Profile

Since its founding, NASA has been dedicated to the advancement of aeronautics and space science. The NASA Scientific and Technical Information (STI) Program plays a key part in helping NASA maintain this important role.

The NASA STI Program operates under the auspices of the Agency Chief Information Officer. It collects, organizes, provides for archiving, and disseminates NASA's STI. The NASA STI Program provides access to the NASA Technical Report Server—Registered (NTRS Reg) and NASA Technical Report Server—Public (NTRS) thus providing one of the largest collections of aeronautical and space science STI in the world. Results are published in both non-NASA channels and by NASA in the NASA STI Report Series, which includes the following report types:

- TECHNICAL PUBLICATION. Reports of completed research or a major significant phase of research that present the results of NASA programs and include extensive data or theoretical analysis. Includes compilations of significant scientific and technical data and information deemed to be of continuing reference value. NASA counter-part of peer-reviewed formal professional papers, but has less stringent limitations on manuscript length and extent of graphic presentations.

- TECHNICAL MEMORANDUM. Scientific and technical findings that are preliminary or of specialized interest, e.g., "quick-release" reports, working papers, and bibliographies that contain minimal annotation. Does not contain extensive analysis.

- CONTRACTOR REPORT. Scientific and technical findings by NASA-sponsored contractors and grantees.

- CONFERENCE PUBLICATION. Collected papers from scientific and technical conferences, symposia, seminars, or other meetings sponsored or co-sponsored by NASA.

- SPECIAL PUBLICATION. Scientific, technical, or historical information from NASA programs, projects, and missions, often concerned with subjects having substantial public interest.

- TECHNICAL TRANSLATION. English-language translations of foreign scientific and technical material pertinent to NASA's mission.

For more information about the NASA STI program, see the following:

- Access the NASA STI program home page at http://www.sti.nasa.gov

- E-mail your question to help@sti.nasa.gov

- Fax your question to the NASA STI Information Desk at 757-864-6500

- Telephone the NASA STI Information Desk at 757-864-9658

- Write to:
  NASA STI Program
  Mail Stop 148
  NASA Langley Research Center
  Hampton, VA 23681-2199

NASA/TM-20205003422

Fatigue Failures at Defective Grains in a Single Crystal Nickel-Base Superalloy

T.P. Gabb, T.M. Smith, J.A. Nesbitt, J. Telesman, and C.A. Kantzos
Glenn Research Center, Cleveland, Ohio

I.E. Locci
University of Toledo, Toledo, Ohio

L.J. Evans and L.J. Ghosn
Glenn Research Center, Cleveland, Ohio

National Aeronautics and
Space Administration

Glenn Research Center
Cleveland, Ohio 44135

October 2020

Acknowledgments

Level of Review: This material has been technically reviewed by technical management.

Available from

This report is available in electronic form at http://www.sti.nasa.gov/ and http://ntrs.nasa.gov/

Fatigue Failures at Defective Grains in a
Single Crystal Nickel-Base Superalloy

T.P. Gabb, T.M. Smith, J.A. Nesbitt,[*] J. Telesman, and C.A. Kantzos
National Aeronautics and Space Administration
Glenn Research Center
Cleveland, Ohio 44135

I.E. Locci
University of Toledo
Toledo, Ohio 43606

L.J. Evans and L.J. Ghosn
National Aeronautics and Space Administration
Glenn Research Center
Cleveland, Ohio 44135

Abstract

Single crystal nickel-base superalloys used as turbine engine blades can have much higher creep and fatigue resistance than many polycrystalline superalloys due to the absence of weak grain boundaries as well as the ability to orient the blades in the primary loading direction on to the low elastic modulus [001] orientation, which significantly lowers the stresses imposed on the blades. However, grain defects can occur in these crystals, impairing these advantages. In the present study, fatigue tests of a single crystal superalloy uncovered unexpected defective grains in the test specimens, which initiated premature fatigue failures. The characteristics of these defective grains and the associated failures were evaluated and related to the observed fatigue lives.

1.0   Introduction

Single crystal nickel-base superalloys used as turbine engine airfoils can have much higher creep and thermal fatigue resistance required for blades and vanes than many polycrystalline superalloys, due to the absence of weak grain boundaries as well as the low elastic modulus in the [001] single crystal growth direction (Refs. 1 and 2). This has allowed increased turbine rim inlet temperatures for improved performance and efficiency. However, these advantages in performance require constraints on acceptable levels of recognized defects in single crystal superalloys (Ref. 3). Single crystal superalloys are usually designed with insufficient carbon, boron, and zirconium to phase or solid solution strengthen grain boundaries as in polycrystalline superalloys. Any grain boundaries that do form could weaken the blades. Macroscopic grains that have grown at high crystallographic angles to the primary grain represent a most serious defect, producing a large grain boundary of known low strength, where the adjacent crystals are at high crystallographic angles to each other ("high angle boundary-HAB"). Macroscopic grains that have grown at sufficiently low crystallographic angles to the primary grain are less detrimental, and can be acceptable "low angle boundaries" (LAB).

---

[*] Currently retired.

Even small casting defect grains or recrystallized grains can introduce such potentially weak grain boundaries into the parent single crystal. Some small casting defect grains can nucleate and grow in chains at the cast surface ("freckles") due to insufficient thermal gradient or growth rate. To check for all these occurrences, single crystal turbine airfoils and other components, very often used with as-cast surfaces, are grain-etched and inspected before and even after heat treatments, to ensure these aspects conform to acceptability limits (Ref. 3).

Studies of various other single crystal superalloys have shown (Refs. 4 and 5) that new grains can recrystallize after casting the single crystal, during heat treatment or during service, at locations which have experienced significant plastic deformation. A systematic study (Ref. 6) of several single crystal superalloys CMSX-6, CMSX-11B, PWA 1483, and SRR 99 indicated low temperature plastic deformation as small as 1 percent is sufficient to encourage subsequent recrystallization at exposed surfaces. Varied annealing heat treatments were not successful in removing enough of this plastic deformation to avoid recrystallization. Surface oxidation was not necessary for recrystallization, as it also occurred in vacuum.

Several studies of this recrystallization problem subsequent to casting have been focused on CMSX-4, which is a very widely used commercially available single crystal nickel based superalloy (Ref. 7). In one illuminating study (Ref. 8), indentations at room temperature and tensile tests at varied temperatures were used to produce plastic strain, and then annealing experiments were performed to study recrystallization tendencies and kinetics. Plastic strains exceeding 1 percent were sufficient to encourage recrystallization in subsequent extended heating to temperatures exceeding 1200 °C. In a focused study (Ref. 9), the effects of indentations on plastic strains at room temperature and subsequent recrystallization tendencies were further studied and modeled. For spherical indentations introduced at room temperature onto single crystal surfaces nearly normal to the [001] crystallographic direction, plastic strains were predicted to extend further in the <011> directions, consistent with the greater extent of subsequent recrystallization in those directions. A later detailed series of experiments and modeling of plastic strains introduced at high temperatures during casting of CMSX-4 (Ref. 10) indicated inelastic strains introduced at stress concentrations from the mold during initial cooling can be sufficiently severe to encourage recrystallization during subsequent heat treatments. This work also showed in more detail how tensile plastic deformation introduced at temperatures above 1200 °C was more effective in promoting recrystallization.

All this work indicates that grain defects in single crystal superalloys can be encountered, even in modern, well-understood alloys and processes. A variance in pattern or mold configuration, casting conditions, rougher handling before heat treatment, or unexpected events during service can encourage the formation of such grain defects. The effects of introduced grain defects on the mechanical properties can be significant (Ref. 11 to 14). Work has shown that low angle grains and their grain boundaries (LAB) with crystallographic orientations less than 8° away from the parent single crystal may have only minor effects on ultimate tensile strength, but sustain failures initiating at the grain boundaries (Ref. 11). Early crack initiation at high angle grains and their grain boundaries (HAB) created transverse to the loading axis has been reported to occur during creep loading (Ref. 12). Grains nucleated along the shot peened surface of another single crystal superalloy were shown to initiate cracks and reduce rupture life, with increasing depth of the grains giving increasing reductions in rupture life (Ref. 13). Other work has shown that recrystallized grains formed within slip bands during thermomechanical fatigue of single crystals initiated fatigue cracks that caused failure (Ref. 14). However, the literature review conducted for this study has not identified previous work detailing the effect of such grain defects on fatigue life of single crystal alloys in isothermal fatigue. The objective of the study was to examine how identified defective grains contained within single crystals influenced fatigue life and failure modes. Single crystal

specimens which contained these defective grains were tested at 815 °C. The effects of the defective grains on fatigue life and failure mode were evaluated.

2.0   Materials and Procedure

The single crystal superalloy test material had a composition in weight percent very similar to that typically reported for CMSX-4 (Ref. 14) cited in many of the above referenced studies of recrystallization, as compared in Table I. Bars of the alloy obtained were approximately 26 mm in diameter and 200 mm in length which had been cast, hot isostatic pressurized, solution heat treated, and aging heat treated using typical industry practices as for CMSX-4. Fatigue test specimens shown in Figure 1 were extracted by electro-discharge machining followed by low stress grinding, with the specimen axial centerlines oriented within 8° of the [001] crystallographic direction. Some of the fatigue specimens were wet blast and the gage sections were coated with a NiCrY coating as described in References 15 and 16. The gage sections of all fatigue specimens were subsequently conditioned using shot peening (SP) at Metal Improvement Company according to AMS 2432 using conditioned cut stainless steel wire (CCW14) at an average intensity of 4 N, and coverage of 100 percent. Here, 100 percent coverage indicates 100 percent of the surface area has been impacted (Ref. 17). Some coated and uncoated specimens were exposed in air at 815 °C for 500 h, coated with salt and then exposed at 815 °C for 50 h, using the techniques as described in References 15 and 16. All fatigue specimens were then fatigue tested at 815 °C with load cycled to produce maximum and minimum cyclic stresses of 841 MPa and –152 MPa at a frequency of 0.33 Hz until failure. Fractures were evaluated using a Nikon optical stereomicroscope and JEOL 6100 scanning electron microscope (SEM). Additional analysis of the fracture surfaces for selected specimens was performed using a Tescan MAIA3 field emission scanning electron microscope (SEM). An Oxford Instruments energy dispersive x-ray spectrometer (EDS) with X-MaxN 50 detector integrated in the Tescan was used to create x-ray maps of the failure initiation point. A NordlysNano electron backscatter diffraction (EBSD) detector integrated in the Tescan was used for determining crystallographic orientations of the failure initiation site and the adjacent single crystal. Surface profiles were generated from stereo pair images of this failure initiation site using MeX image analysis software. Dimensions of all presented failure sites were measured using SigmaScan Pro image analysis software. Fatigue crack growth lives were estimated from images of each fracture surface using NASGRO software.

TABLE I.—COMPOSITION IN WEIGHT PERCENT OF TESTED ALLOY VERSUS CMSX-4 (REF. 14)
AND LDS-1101+Hf (REF. 19) SINGLE CRYSTAL SUPERALLOY

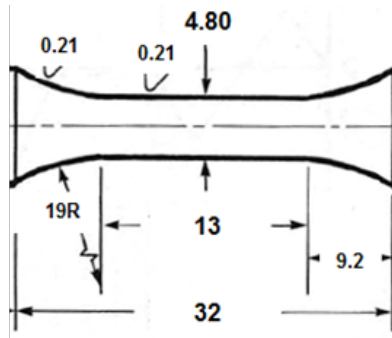| Alloy, wt.%	Al	B	C	Co	Cr	Hf	Mo	Ni	Re	Si	Ta	Ti	W	Y	Zr	Note
Tested alloy	5.035		0.003	10.0	5.40	0.1	1.75	Bal.	3.065	0.04	8.725	0.99	5		0.006	
CMSX-4	5.6			9	6.5	0.1	0.60	Bal.	3		6.5	1.0	6			Ref. 7
LDS-1101+Hf	6.1		0.024	10	5	0.19	7.30	Bal.	3.1		6.50			0.0078		Ref. 19

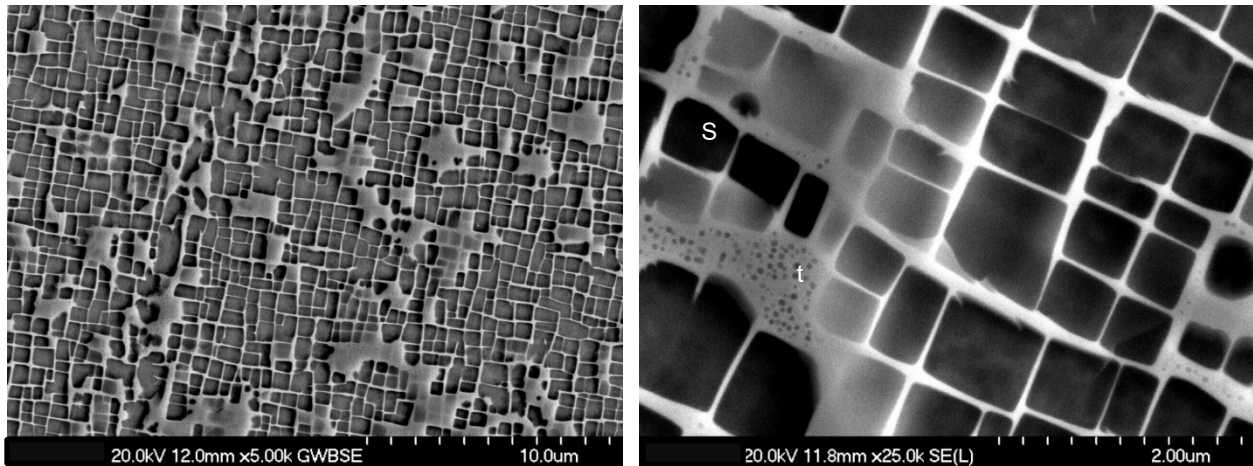Figure 1.—Fatigue test specimen gage configuration, with dimensions in mm.

Figure 2.—Typical microstructure of the single crystal superalloy tested, showing larger cuboidal secondary (S) and smaller spherical tertiary (t) γ' precipitates.

3.0 Results

3.1 Microstructure

The typical microstructure of the single crystal superalloy tested is shown in Figure 2. Cuboidal secondary γ' precipitates had an average cube width of 0.49 μm, while spherical tertiary γ' precipitates had an average width of 0.05 μm.

3.2 Fatigue Failure Initiation Sites

Many tested specimens had fatigue lives ranging from 54,569 to 273,873 cycles. Those specimens failed from surface oxidation or internal inclusions. However, another group of specimens had appreciably lower fatigue lives of 934 cycles to 26,883 cycles, and displayed an unusual, consistent failure mode. Optical images of the latter specimen fractures are shown with the associated fatigue lives in Figure 3. These uncoated or coated, unexposed or exposed specimens failed from significantly larger crack initiation sites than the prior specimens. Within each subgroup of coated, unexposed and coated, exposed specimens, the fatigue life tended to decrease with increasing size of the failure initiation site.
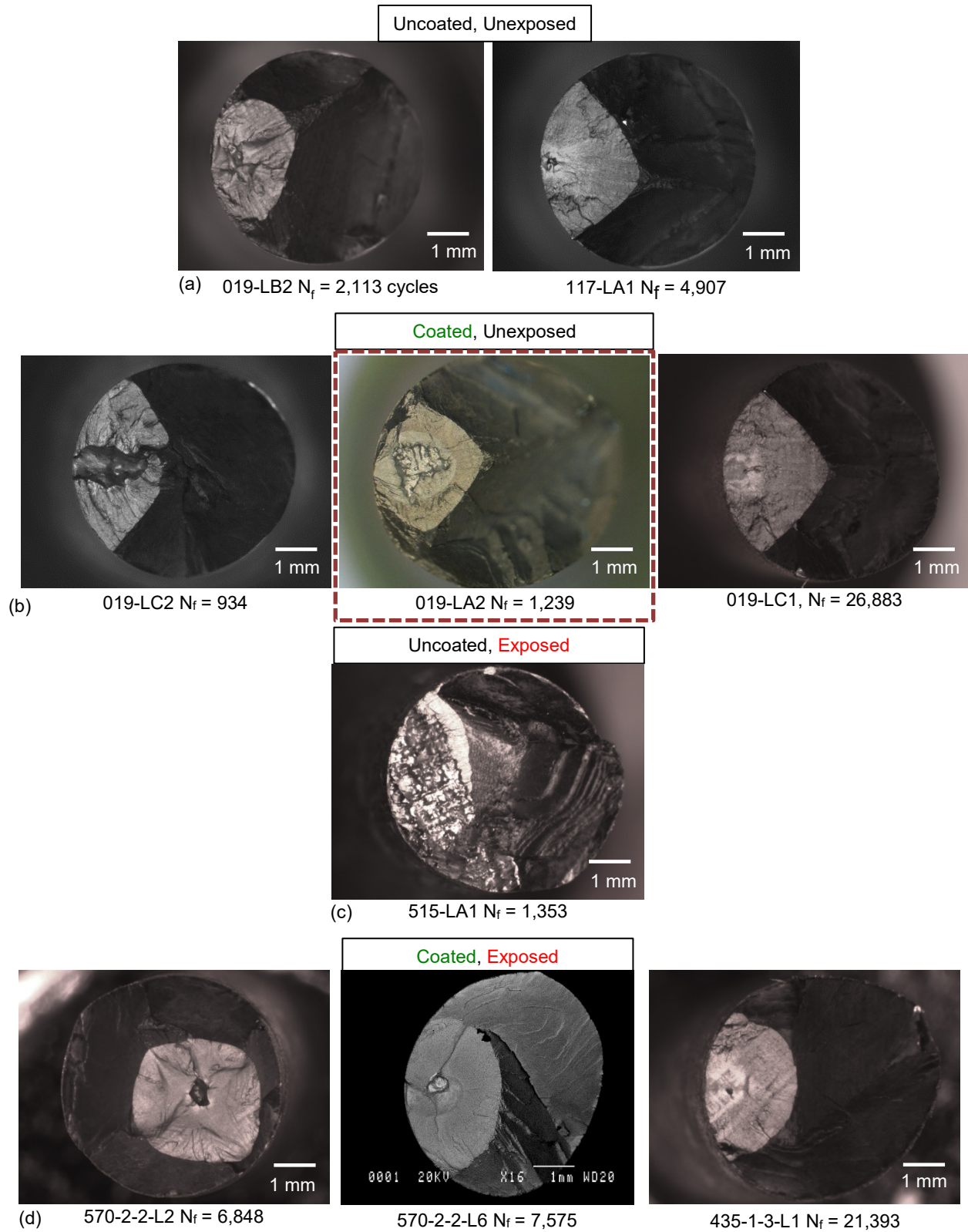
Figure 3.—Fatigue failures with unusual failure initiation sites: (a) uncoated, unexposed, (b) coated, unexposed, (c) uncoated, exposed, (d) coated, exposed.

The first failure encountered in this group was studied in detail. Optical and SEM images of this fracture surface are shown in Figure 4. Stereo pair images of each mating surface of the fracture ("conjugate") were analyzed using MeX software in order to determine surface profiles of each half. The line profiles in Figure 5 match well and indicate this failure initiation site was not a void, but was a large embedded feature. The backscattered electron imaging mode is sensitive to average atomic number of the surface, so these images also suggested the overall average atomic number of the feature is comparable to that of the superalloy.

The composition of the large feature was further evaluated in the Tescan MAIA3 SEM using the Oxford EDS in the x-ray elemental mapping mode. The resulting chemical maps are presented for different elements in Figure 6. The maps indicate the defect, in comparison to the adjacent single crystal, had higher amounts of Co and Ni, and relatively lower levels of the elements Cr, Mo, Ta, Re, W, and Al. As shown in Table II, preliminary composition measurements of the feature indicated increased levels of Co and Ni, and decreased levels of Cr, Mo, Re, W, and Al. The changes were near 2 wt.% for most elements, however the decrease in Al was over 4 wt.%. It is noted that surface roughness may influence x-ray signal strength, and this could not be compensated for in these maps. In future work, attempts will be made to prepare a metallographic section through the defective grain to produce a flat, unoxidized surface for further evaluations of its composition.
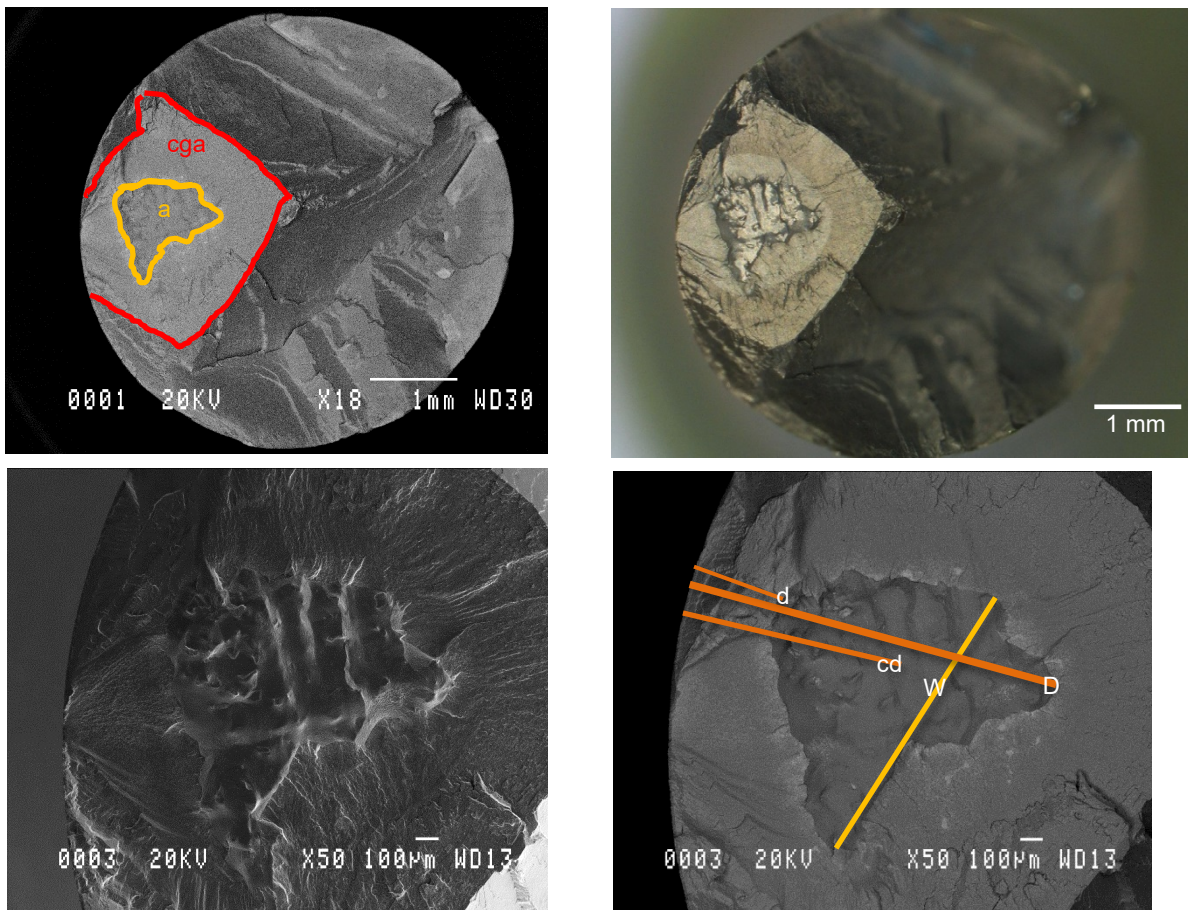

Figure 4.—First specimen to fail from this mode: coated, unexposed specimen 019-LA2 failed at 1,239 cycles. Measurements are annotated with lines: maximum width (W), minimum depth (d), maximum depth (D), centroid depth (cd), defective grain area (a), total crack growth area (cga).
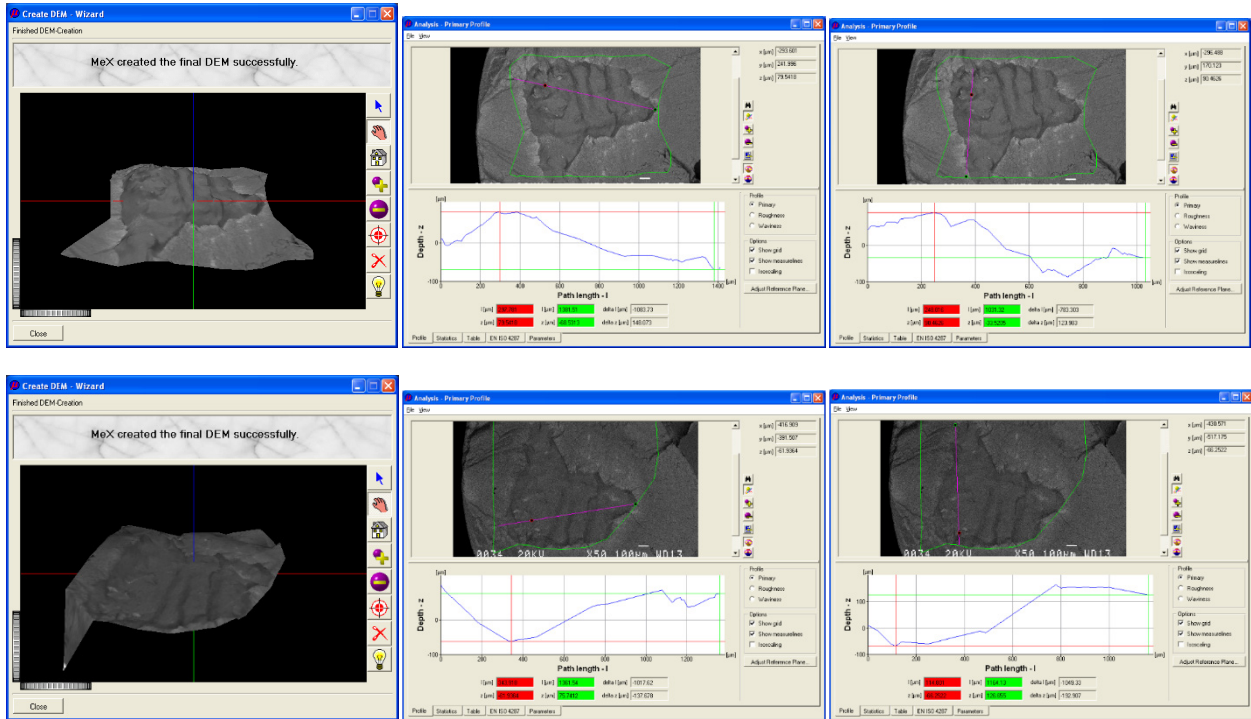
Figure 5.—Matching line profiles for conjugate fracture surfaces of specimen 019-LA2 from Figure 4 and Figure 3.
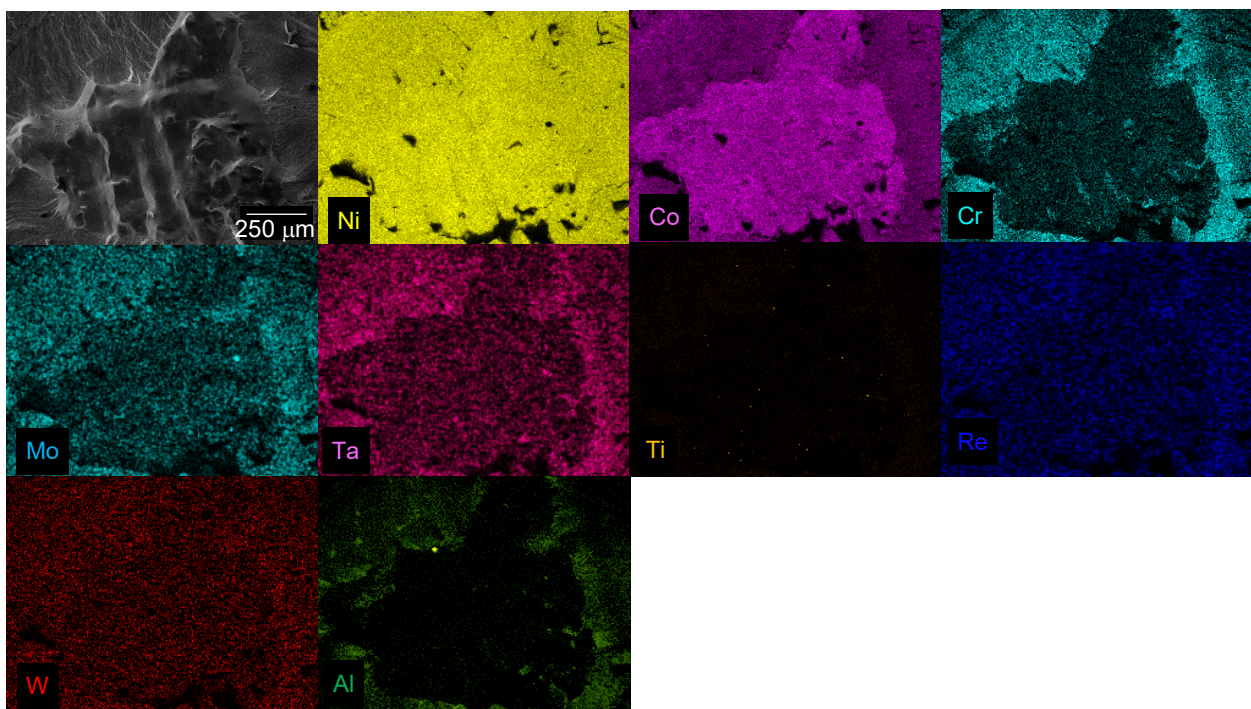

Figure 6.—SEM X-ray maps indicating differences in composition between the defective grain and the single crystal.

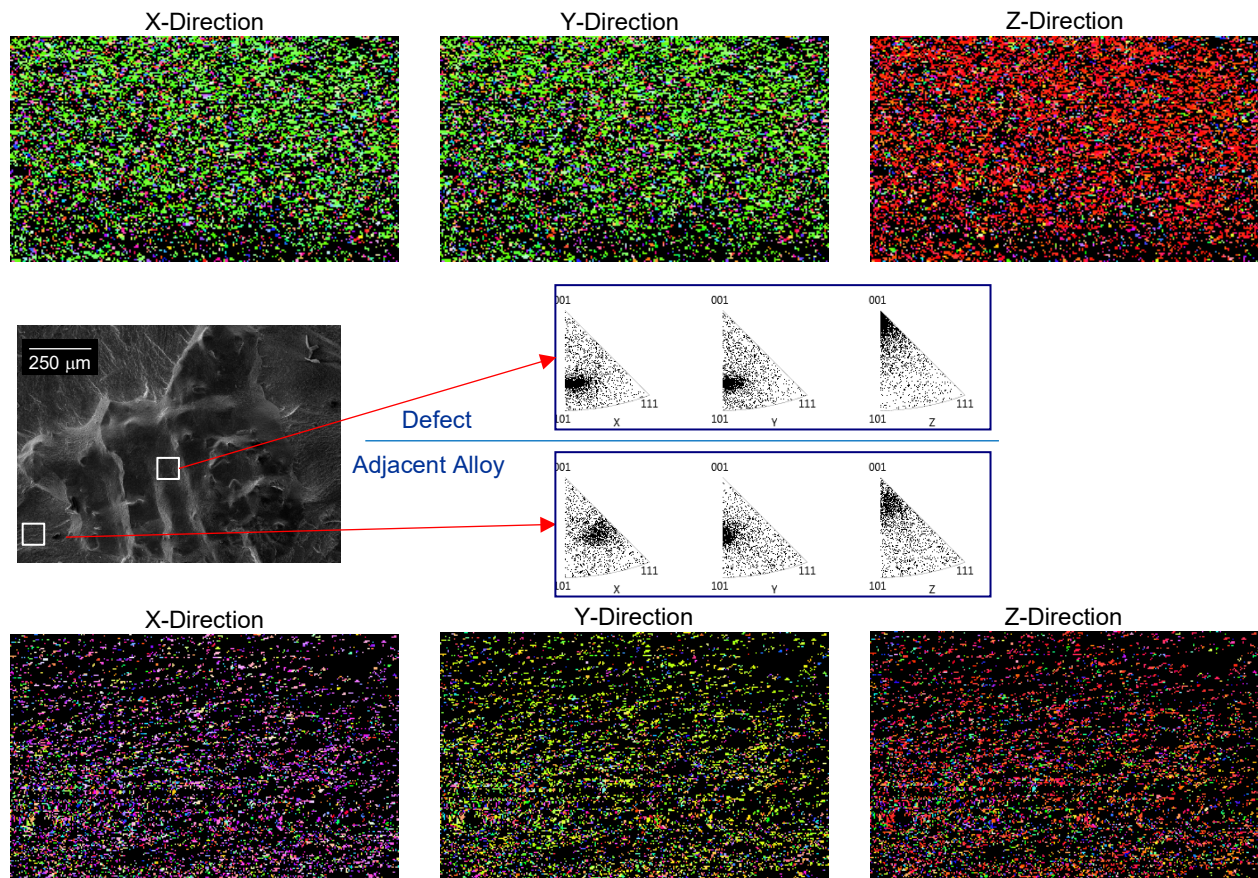| Alloy, wt.%	Al	B	C	Co	Cr	Hf	Mo	Ni	O	Re	Si	Ta	Ti	W	Y	Zr
Single crystal alloy	5.325		0.000	10.860	5.313	0.000	1.236	Bal.	2.438	0.000	0.000	9.070	0.879	2.857	0.000	0.000
Defective grain	0.939		0.000	12.014	2.703	0.000	0.740	Bal.	5.122	0.000	0.000	7.695	0.794	2.667	0.000	0.000

Figure 7.—Electron back scatter diffraction pattern indicating difference in crystallographic orientation between the defective grain and single crystal.

Electron backscattered diffraction (EBSD) was also used to compare the crystallographic orientation of the feature to that of the surrounding single crystal superalloy. Though the rough, unpolished surface added significant noise to this analysis, the feature clearly had an overall different crystallographic orientation than the surrounding single crystal superalloy as shown by the inverse pole figure maps in Figure 7. Based on these evaluations, the large feature that initiated this failure can be described as a defective processing grain of different crystallographic orientation and somewhat modified composition, with respect to those aspects of the surrounding single crystal superalloy. Key dimensions of the defective grain were measured and tabulated, including area (a), maximum width (W), transverse width, minimum depth (d), maximum depth (D), and centroid depth (cd). The flat area normal to the loading direction which surrounded the grain appeared to represent the region of stable crack growth after crack initiation and before final failure. The final failure occurred by shearing on large crystallographic planes at high

angles to the loading axis. This flat area encompassing both fatigue crack initiation and fatigue crack growth was also measured (cga). Each dimension is illustrated on Figure 4.

The other fractures from this group of specimens with low lives were also imaged and are shown in Figure 8 to Figure 15. In most cases, comparison of the conjugate fracture surfaces indicated a defective grain of similar morphology was embedded in one half of the fracture, as previously described. The largest defective grain with a maximum width of 3.322 mm was observed for an uncoated, exposed specimen shown in Figure 10. The smallest defective grain with a maximum width of 0.096 mm was observed for a coated, unexposed specimen shown in Figure 12. One interesting exception is shown in Figure 11, a relatively large feature of similar appearance was observed, but neither surface had the grain remaining. This suggested that either the defective grain had fallen out or this feature could be a large pore, even though it does not contain typical features associated with pores. For all these fracture surfaces, the same key dimensions of the failure initiation sites were measured and tabulated, including defective grain area, grain maximum width, grain minimum depth, grain maximum depth, grain centroid depth, and total fatigue cracked area. These measured dimensions are summarized in Table III.
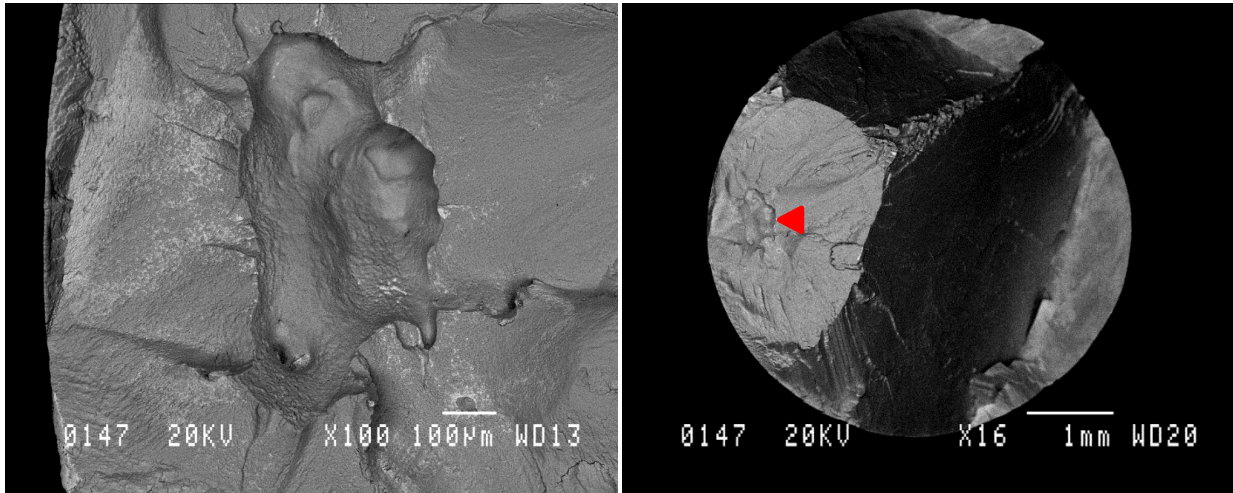

Figure 8.—Uncoated, unexposed specimen 019-LB2 failed at 2,113 cycles from a near-surface defective grain 0.75 mm in maximum width.
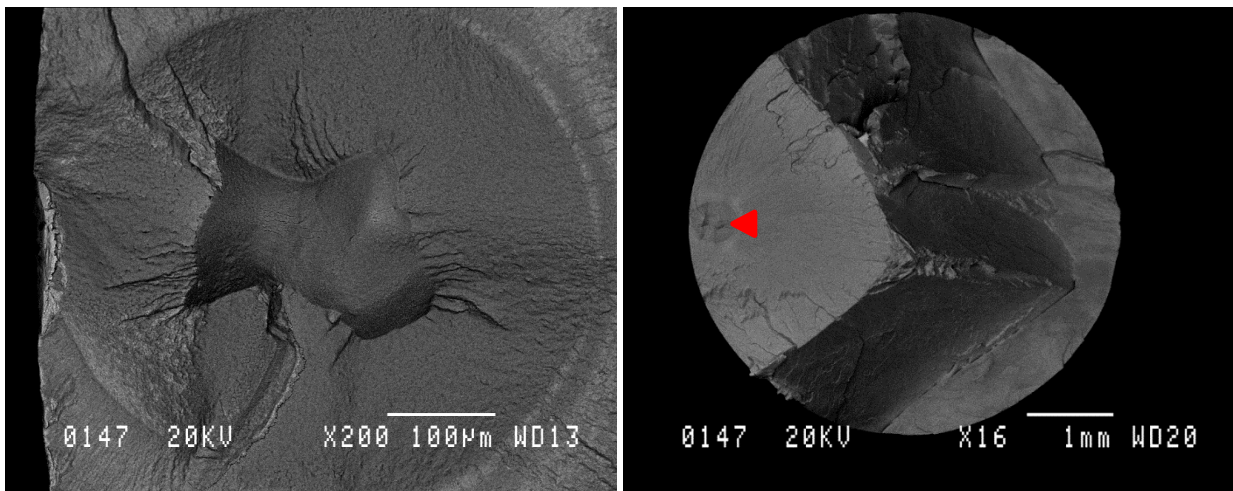

Figure 9.—Uncoated, unexposed specimen 117-LA1 failed at 4,907 cycles from a near-surface defective grain 0.25 mm in maximum width.
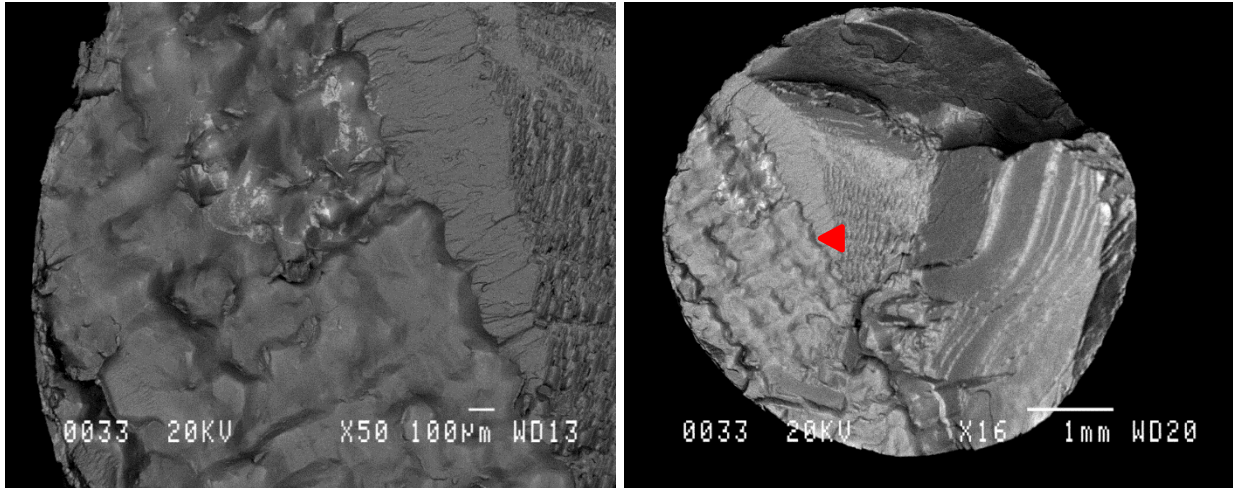
Figure 10.—Uncoated, exposed specimen 515-LA1 failed at 1,353 cycles from a surface defective grain 3.32 mm in maximum width.

Figure 11.—Coated, unexposed specimen 019-LC2 failed at 934 cycles from a surface defective grain 1.80 mm in maximum width.
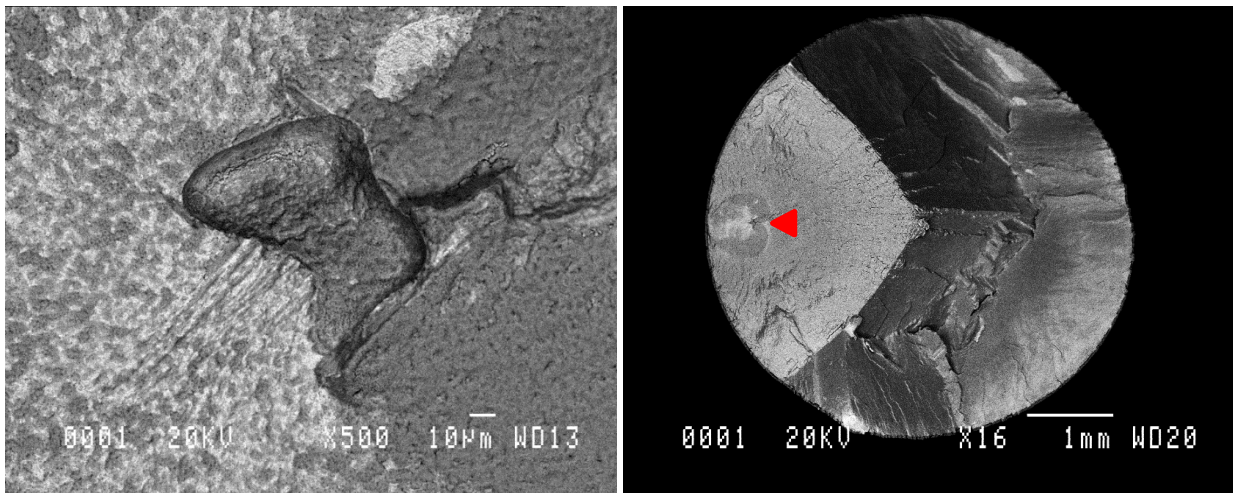

Figure 12.—Coated, unexposed specimen 019-LC1 failed at 26,883 cycles from an internal defective grain 0.096 mm in maximum width.
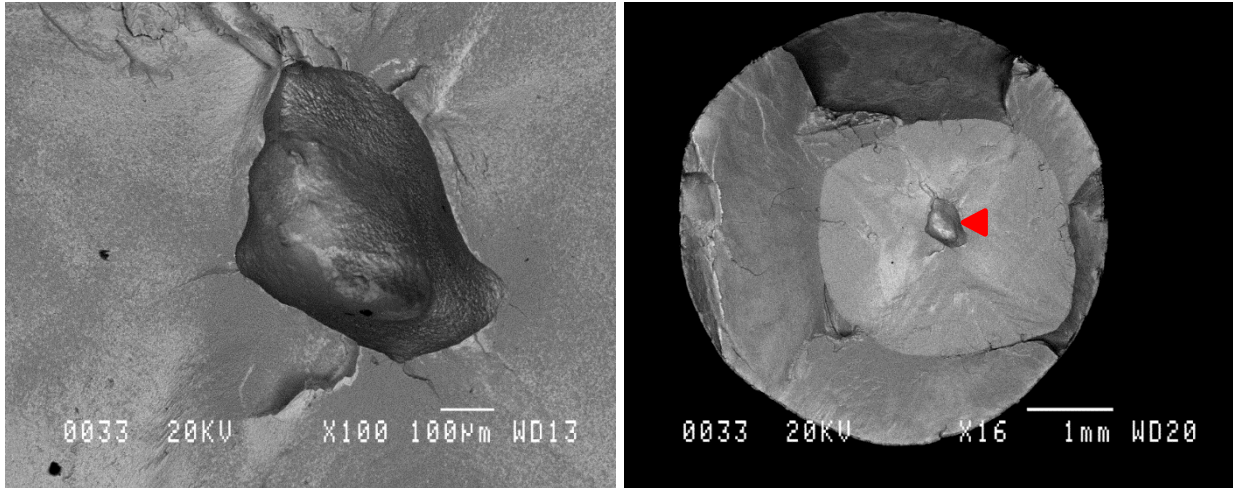
Figure 13.—Coated, exposed specimen 570-2-2-L2 failed at 6,848 cycles from an internal defective grain 0.64 mm in maximum width.
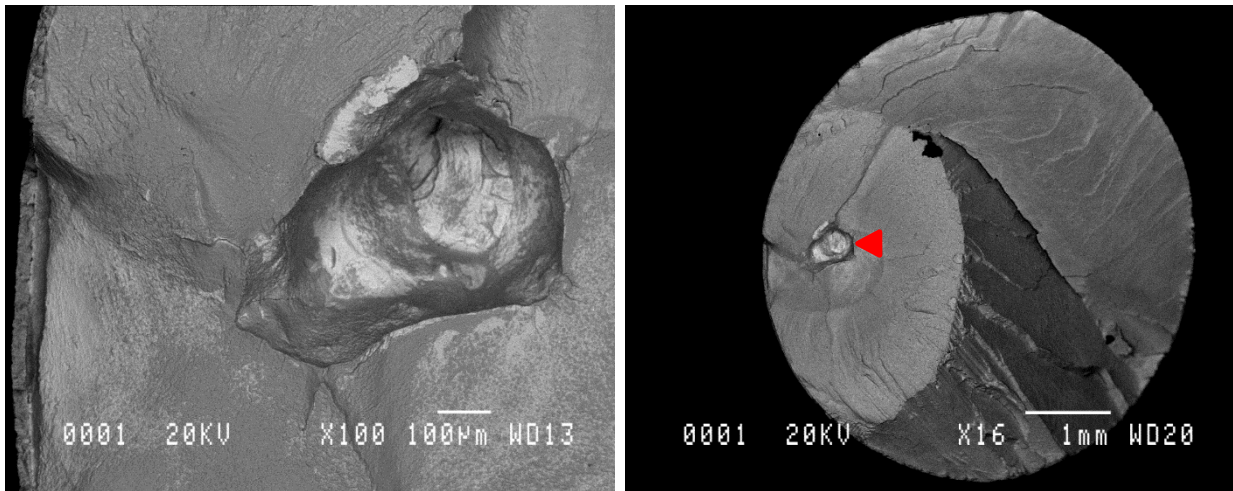

Figure 14.—Coated, exposed specimen 570-2-2-L6 failed at 7,575 cycles from a near-surface defective grain 0.66 mm in maximum width.
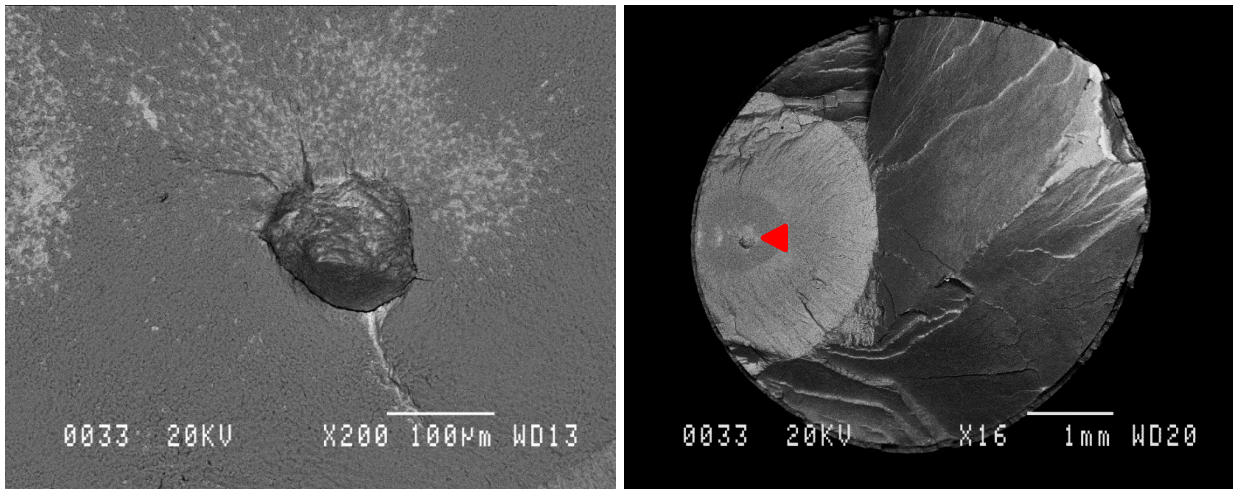

Figure 15.—Coated, exposed specimen 435-1-3-L1 failed at 21,393 cycles from an internal defective grain 0.15 mm in maximum width.

TABLE III.—DIMENSIONS MEASURED FROM DEFECTIVE GRAIN
AND INCLUSION (YELLOW) INITIATED FAILURES

Sample	Coated	Peened	Exposed	Heat treated	Fatigue life Nf	Log (life)	Defect area, mm^2	Defect max width, mm	Defect min depth, mm	Defect max depth, mm	Centroid depth, mm	Crack growth area, mm^2	Comments
019-LA2	NiCrY	4N-100%	No	760 °C 8H low pO$_2$	1,239	3.0931	0.833	1.296	0.378	1.66	1.185	4.458	Defective grain
019-LB2	Uncoated	4N-100%	No	760 °C 8H low pO$_2$	2,113	3.3249	0.195	0.751	0.377	0.741	0.447	4.615	Defective grain
019-LC1	NiCrY	4N-100%	No	760 °C 8H low pO$_2$	26,833	4.4287	0.004	0.096	0.462	0.544	0.522	5.618	Defective grain
019-LC2	NiCrY	4N-100%	No	760 °C 8H low pO$_2$	934	2.9703	1.231	1.788	0.01	1.796	0.662	5.772	Surface flaw/defective grain
117-LA1	Uncoated	4N-100%	No	760 °C 8H low pO$_2$	4,907	3.6908	0.026	0.249	0.129	0.363	0.258	5.567	Defective grain
515-LA1	Uncoated	4N-100%	Yes	760 °C 8H low pO$_2$	1,353	3.1313	4.21	3.322	0.01	1.827	1.060	7.065	Defective grain-surface flaw/initial crack too large for valid analysis
520-2-2-L2	NiCrY	4N-100%	Yes	760 °C 8H low pO$_2$	6,848	3.8356	0.197	0.642	1.58	2.133	1.817	6.728	Fully internal initiation and crack growth at defective grain
570-2-2-L6	NiCrY	4N-100%	Yes	760 °C 8H low pO$_2$	7,575	3.8794	0.199	0.662	0.412	1.013	0.842	6.727	Defective grain
435-1-3-L1	NiCrY	4N-100%	Yes	760 °C 8H low pO$_2$	21,393	4.3303	0.014	0.15	0.515	0.663	0.600	4.984	Defective grain
034-LA2	Uncoated	4N-100%	No	760 °C 8H low pO$_2$	231,555	5.3647	0.00055	0.030	0.436	0.465	0.449	5.90920	Inclusion
034-LA1	NiCrY	4N-100%	Yes	760 °C 8H low pO$_2$	198,398	5.2975	0.00072	0.041	0.183	0.223	0.209	5.91962	Inclusion

Regressions were performed in order to determine which factors in Table III were correlated with fatigue life. No significant correlations were detected between life and the presence of a coating or the application of oxidation plus hot corrosion exposures. No significant correlation was detected between fatigue life and total fatigue cracked area. However, significant relationships existed between fatigue life and dimensions of the defective grains. Fatigue life clearly decreased with increasing defective grain width and with increasing defective grain area, as shown in Figure 16. Therefore, the defective grains strongly influenced fatigue life, and they could be considered life-limiting defects.

The fracture surfaces of two fatigue specimens having much longer fatigue lives are shown in Figure 17 and Figure 18 for comparison purposes. The failure initiation site of an uncoated, unexposed specimen that failed at 231,555 cycles is shown in Figure 17. This specimen failed from an internal aluminum-rich non-metallic oxide inclusion having a maximum width of 0.030 mm. The failure of a coated, exposed specimen that failed at 198,398 cycles is shown in Figure 18. This failure was also from an internal aluminum-oxide inclusion, having a maximum width of 0.041 mm.
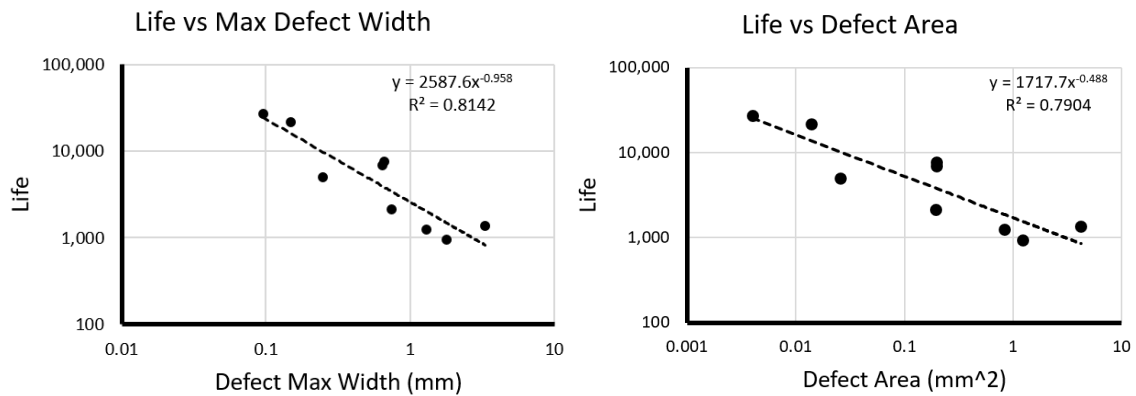

Figure 16.—Significant relationships existed between fatigue life in cycles and grain dimensions: life decreased with increasing defective grain width and area. No significant relationships were detected between fatigue life and presence of a coating or application of the exposures.
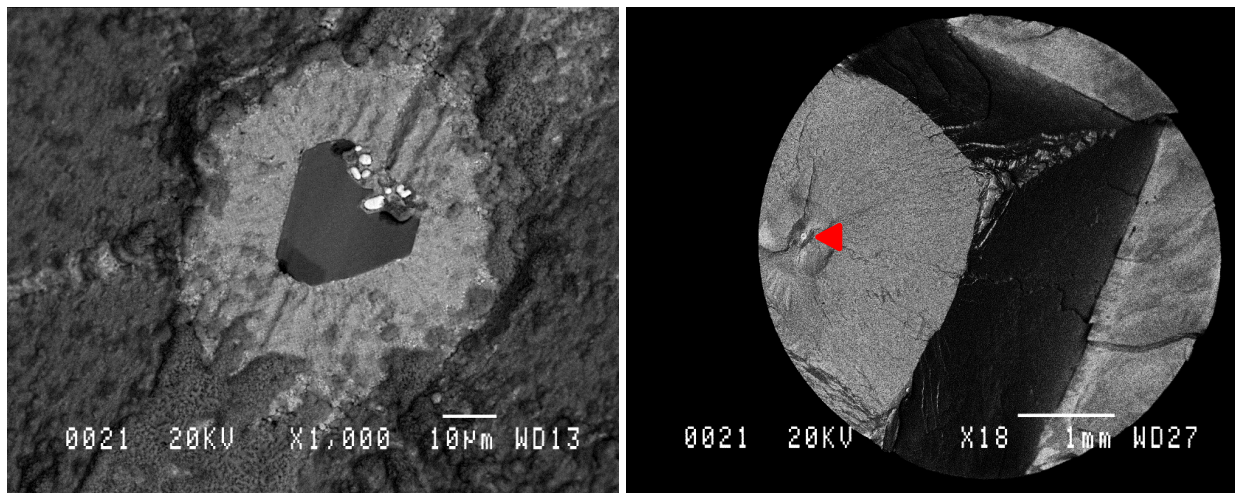

Figure 17.—Uncoated, unexposed specimen 034-LA2 failed at 231,555 cycles from an internal aluminum-rich oxide inclusion 0.030 mm in maximum width.
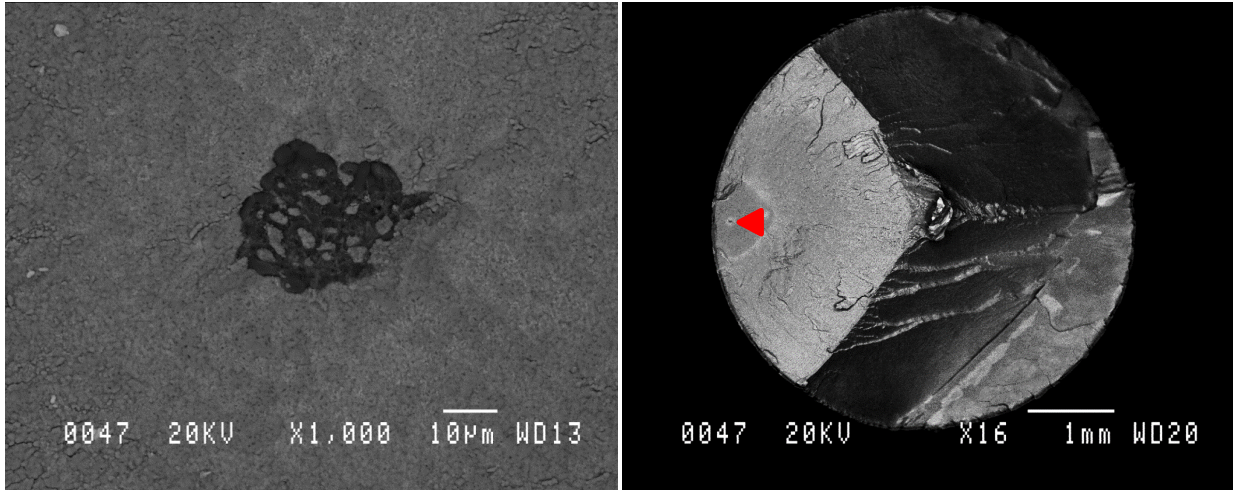
Figure 18.—Coated, exposed specimen 034-LA1 failed at 198,398 cycles from an internal aluminum-oxide inclusion 0.041 mm in maximum width.

The areas of flat crack growth surrounding the inclusions were very similar, and the total areas of fatigue cracking in these specimens were comparable to those of the prior specimens failing at defective grains, as also listed in Table II. Since the total area of fatigue cracking appeared comparable for all these specimens, it was valid and of interest to estimate the number of cycles necessary to grow each fatigue crack from the circumference of the crack initiation site across the flat area to the final shear crystallographic facet failure. In this way, the portion of each fatigue failure life attributable to crack growth could be compared.

3.3   Estimated Crack Growth Lives

The NASGRO 9.0 (Ref. 17) fracture mechanics and fatigue crack growth prediction code was used to estimate crack growth response of all these presented specimens. No fracture mechanics solution existed in NASGRO for internal flaws in cylindrical specimens. Instead, a specimen geometry with a square cross section of the same width as the diameter of the actual fatigue test specimens was employed, as shown in Figure 19. This NASGRO solution allows for the flaw location and aspect ratio to be similar to those measured on the fracture surfaces of the failed specimens. For surface flaws in cylindrical specimens, the same situation occurred, and so the available surface flaw geometry shown in Figure 20 was employed, again using a square cross section having the same width as the fatigue specimen diameter.

NASGRO requires input of a crack growth equation as a function of the applied stress intensity range. A Paris regime equation was fitted to the only available single crystal test data set performed at similar conditions as those of the LCF tests, as shown in Figure 21. This test was performed on a single crystal superalloy NASA LDS-1101+H_f (Ref. 18) specimen oriented near the [001] crystallographic direction, with $R_{min/max\ stress} = 0.05$ and frequency of 0.333 Hz in air. As shown in Table I, this tested superalloy was judged to have a sufficiently similar composition to that of the present alloy, and so the test data was applied here. The test data set did not extend into the threshold regime and thus a conservative approach of strictly using only the Paris regime relationship was used. This is in line with much of the small crack growth data literature which does not use the long crack FCG thresholds in the belief that they are a product of the buildup of crack closure in the crack wake of the long crack growth tests (Refs. 19 and 20). While internal cracks would not be exposed to air until breaching the specimen surface, no data was available for fatigue cracks growing in vacuum. Therefore the crack growth relationship generated in air was also applied for internal cracks, which was also thought to be a conservative approach.
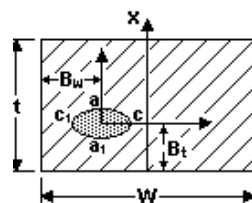
EC05
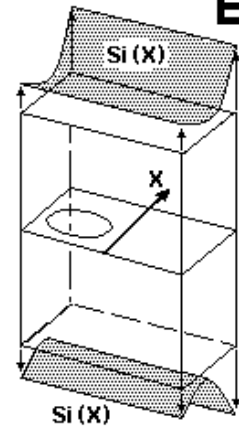
$$S0 = S0(X) = 1$$

$$S1 = 6M_1 / Wt^2$$
$$S1(X) = S1(1 - 2X/t)$$

$$Si^{WF} = Si(X)$$
$$Si^{POLY} = \Sigma C_i (X/t)^i$$

$$0 \le a/Min(B_t, t - B_t) \le 0.99$$
$$0 \le c/Min(B_w, W - B_w) \le 0.99$$
$$0.01 \le a/c \le 10$$

$$0.0 \le X \le 1.0$$

Figure 19.—Internal flaw specimen geometry EC05 available and applied in NASGRO. No solution was available in NASGRO for an internal flaw in a cylindrical specimen. This geometry with a square cross section of the same width as the actual fatigue test specimens was employed. The solution allowed one to set flaw location and aspect ratio to approximate each observed fracture surface.

SC30
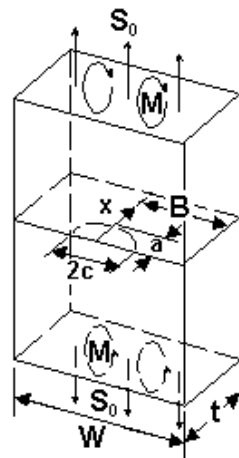
$$S_1 = 6M / Wt^2$$

$$\frac{c}{Min(B, |W - B|)} < 0.95$$

$$0 \le a/t \le 0.95$$
$$0 \le a/c \le 8$$

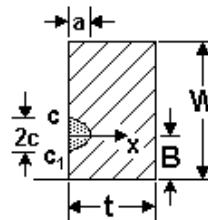$$X = x/t, \quad 0 \le X \le 1$$
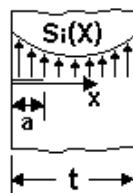
$$Si(X), \quad i = 0, 1, 2, 3$$

Figure 20.—Surface flaw specimen geometry SC30 available and applied in NASGRO.

LDS-1101+Hf [001] Orientation
815 °C, 0.333 Hz, R=0.05

$da/dN=6.37e\text{-}10(\Delta K)^{232}$

LDS 7GG-S2
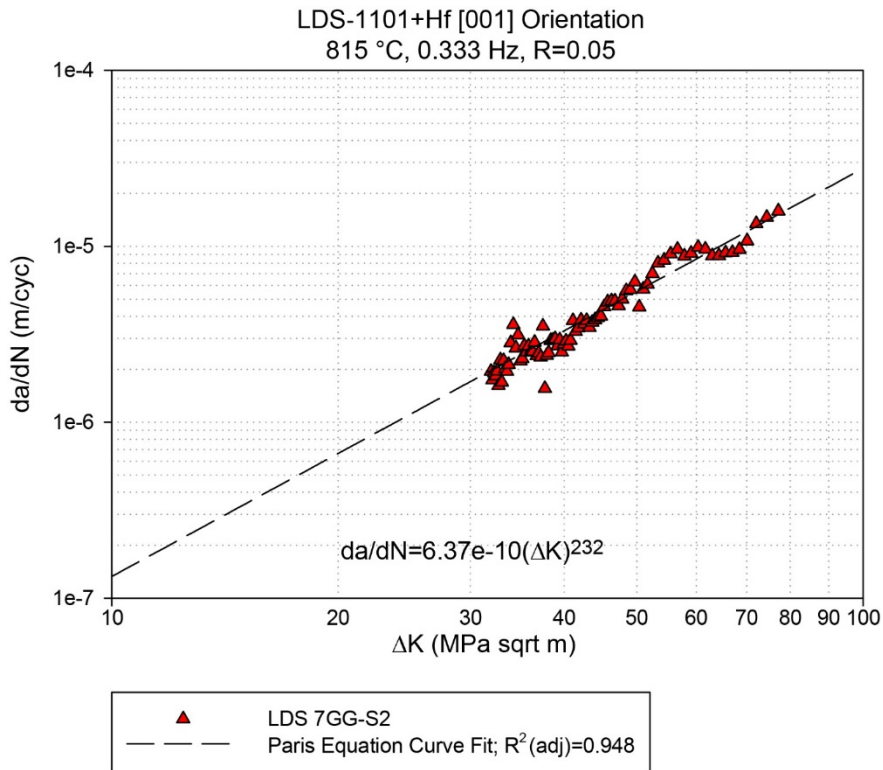Paris Equation Curve Fit; R^2(adj)=0.948

Figure 21.—Input crack growth rate versus stress intensity range test data and relationship used in NASGRO, generated in a single test of NASA LDS-1101+Hf specimen oriented near the [001] crystallographic direction, with $R_{min/max\ stress}$ = 0.05 and frequency of 0.33 Hz in air at 815 °C.

Typical examples of the NASGRO generated crack size versus cycles are compared in Figure 22 for two of the specimens failing at defective grains. In Figure 22(a), crack growth remained internal to the specimen surface all the way to failure, so NASGRO continued crack growth calculations only using the internal flaw geometry illustrated in Figure 19. In Figure 22(b), the crack grew to reach the surface at the number of cycles indicated by the arrow. At that arrow, NASGRO automatically shifted from the internal flaw geometry of Figure 19 to the surface flaw geometry illustrated in Figure 20 for crack growth calculations.

The calculated number of cycles expended by crack growth before failure are compared with overall fatigue life (Nf) in Table IV. The fraction of crack growth/Nf cycles is also listed, and this is shown versus cycles to failure in Figure 23. The results for specimen failing from defective grains shown in Figure 23 indicated a higher fraction of life was taken up by crack growth for larger defective grains to give shorter fatigue life. The results for all specimens including failures initiating at grains and at inclusions indicate a consistent trend across both failure initiation sites, with a high coefficient of determination R^2. Referring to Table IV and the summary Table V, it is clear that crack propagation accounts for a much lower fraction of fatigue life for specimens failing from the relatively small internal inclusions. Hence, the presence of defective grains appears to be more detrimental to fatigue life than the presence of inclusions.
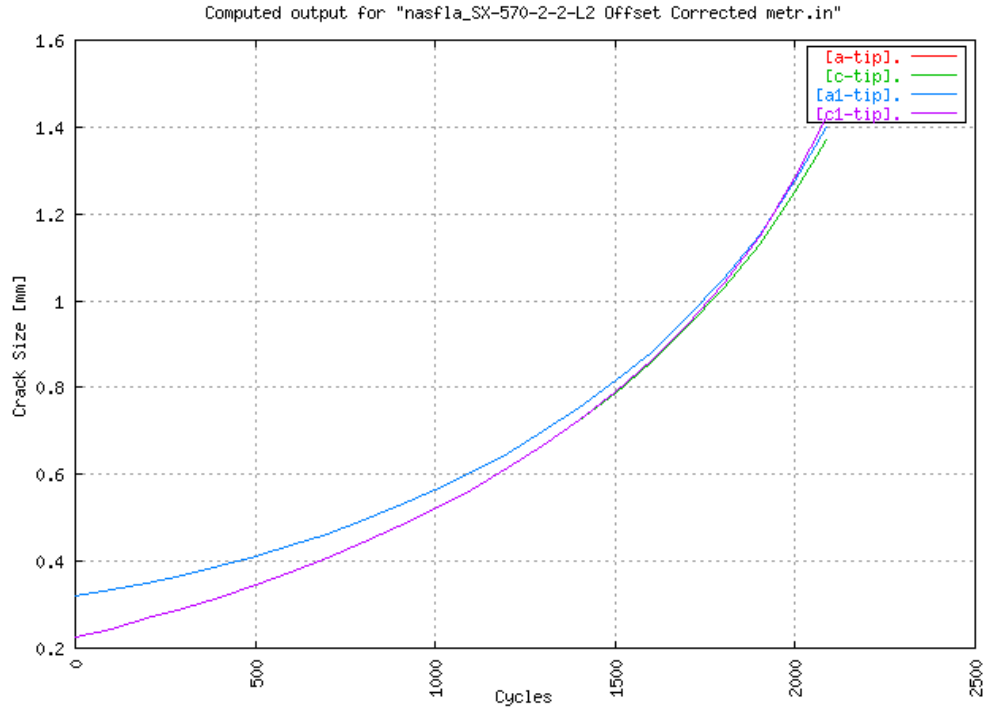
(a)

(b)
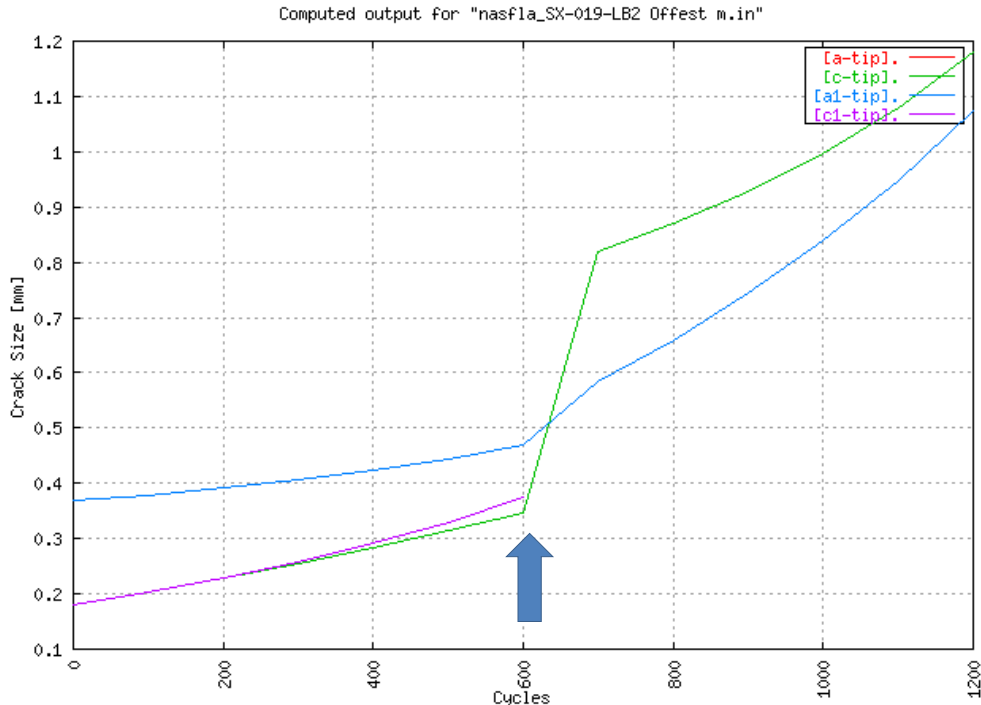
Figure 22.—Typical examples of the crack length versus cycles calculated in NASGRO for two of the specimens failing at defective grains, (a) crack growth remained internal to the specimen surface all the way to failure, (b) the crack grew to reach the surface at the number of cycles indicated by the arrow. At that arrow, NASGRO automatically shifted from the internal flaw geometry of Figure 19 to the surface flaw geometry illustrated in Figure 20 for crack growth calculations.

TABLE IV.—CRACK GROWTH LIFE CALCULATED FOR DEFECTIVE
GRAIN AND INCLUSION (YELLOW) INITIATED FAILURES

| Spec.	Fat life Nf	NASGRO crack growth life	Crack growth/Nf	Comments
019-LA2	1,239	648	0.523002	Defective grain
019-LB2	2,113	1,298	0.614292	Defective grain
019-LC1	26,883	4,655	0.173158	Defective grain
019-LC2	934	558	0.59743	Surface flaw/defective grain
117-LA1	4,907	2,689	0.547993	Defective grain
515-LA1	1,353	Not analyzed		Defective grain-surface flaw/initial crack too large for valid analysis
570-2-2-L2	6,848	2,084	0.304322	Fully internal initiation and crack growth at defective grain
570-2-2-L6	7,575	1,594	0.210429	Defective grain
435-1-3-L1	21,393	3,669	0.171505	Defective grain
034-LA2 (i)	231,555	7,404	0.031975	Inclusion initiation
034-LA1 (i)	198,398	6,331	0.031911	Inclusion initiation
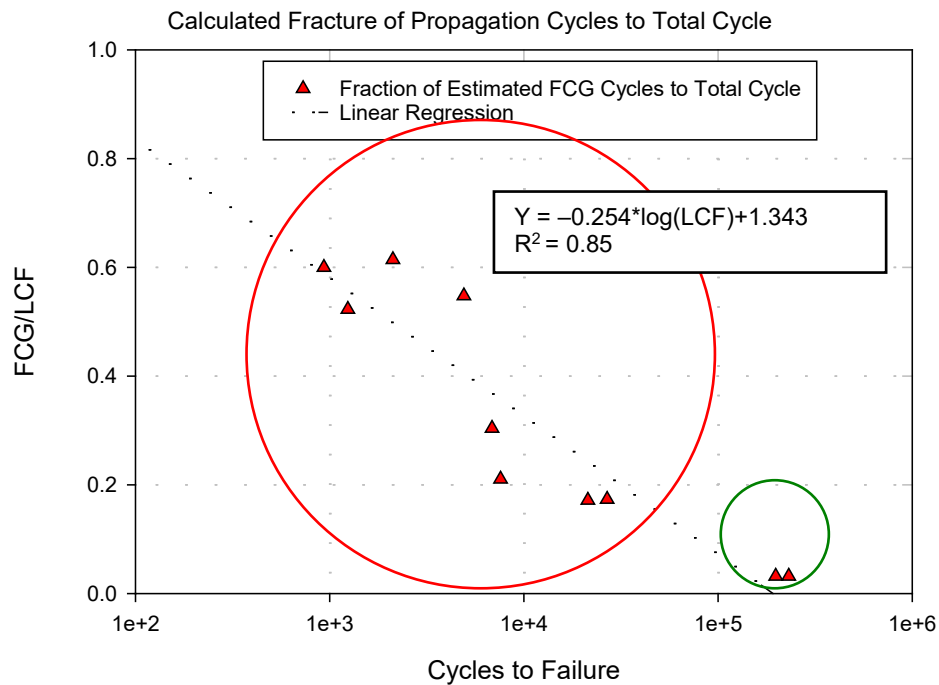
Figure 23.—Fraction of crack propagation cycles to total cycles versus cycles to failure from defective grains (red circle) and from inclusions (green circle).

TABLE V.—SUMMARY OF FEATURE MEASUREMENTS AND CRACK GROWTH LIFE CALCULATED
FOR DEFECTIVE GRAIN AND INCLUSION (YELLOW) INITIATED FAILURES

Sample	Coated	Peened	Exposed	Heat treated	Fatigue life Nf	Log (life)	Defect area, mm^2	Defect max width, mm	Defect min depth, mm	Defect max depth, mm	Centroid depth, mm	Crack growth area, mm^2	NASGRO propagation life	Crack growth/Nf	Comments
019-LA2	NiCrY	4N-100%	No	760 °C 8H low pO$_2$	1,239	3.0931	0.833	1.296	0.378	1.66	1.185	4.458	648	0.523002	Defective grain
019-LB2	Uncoated	4N-100%	No	760 °C 8H low pO$_2$	2,113	3.3249	0.195	0.751	0.377	0.741	0.447	4.615	1,298	0.614292	Defective grain
019-LC1	NiCrY	4N-100%	No	760 °C 8H low pO$_2$	26,833	4.4287	0.004	0.096	0.462	0.544	0.522	5.618	4,655	0.173158	Defective grain
019-LC2	NiCrY	4N-100%	No	760 °C 8H low pO$_2$	934	2.9703	1.231	1.788	0.01	1.796	0.662	5.772	558	0.59743	Surface flaw/ defective grain
117-LA1	Uncoated	4N-100%	No	760 °C 8H low pO$_2$	4,907	3.6908	0.026	0.249	0.129	0.363	0.258	5.567	2,689	0.547993	Defective grain
515-LA1	Uncoated	4N-100%	Yes	760 °C 8H low pO$_2$	1,353	3.1313	4.21	3.322	0.01	1.827	1.060	7.065	Not analyzed		Defective grain-surface flaw/initial crack too large for valid analysis
520-2-2-L2	NiCrY	4N-100%	Yes	760 °C 8H low pO$_2$	6,848	3.8356	0.197	0.642	1.58	2.133	1.817	6.728	2,084	0.304322	Fully internal initiation and crack growth at defective grain
570-2-2-L6	NiCrY	4N-100%	Yes	760 °C 8H low pO$_2$	7,575	3.8794	0.199	0.662	0.412	1.013	0.842	6.727	1,594	0.210429	Defective grain
435-1-3-L1	NiCrY	4N-100%	Yes	760 °C 8H low pO$_2$	21,393	4.3303	0.014	0.15	0.515	0.663	0.600	4.984	3,669	0.171505	Defective grain
034-LA2	Uncoated	4N-100%	No	760 °C 8H low pO$_2$	231,555	5.3647	0.00055	0.030	0.436	0.465	0.449	5.90920	7,404	0.031975	Inclusion
034-LA1	NiCrY	4N-100%	Yes	760 °C 8H low pO$_2$	198,398	5.2975	0.00072	0.041	0.183	0.223	0.209	5.91962	6,331	0.031911	Inclusion

3.4   Potential Methods to Detect the Grains

These defective grains were determined to be serious life-limiting defects. Thus the detection of the defective grains using various evaluation techniques would be highly desirable. The inspection records generated of the bars containing these defects were evaluated. The bars had been radiographed after directional solidification, hot isostatic pressurization, and solution heat treatment were all completed. These records provided no indications that radiography had found pores or voids in any of the bars. Radiography might not be expected to find the presence of such internal defective grains given their relatively small sizes, keeping in mind the large size of each bar being inspected. The bars had also been macro-etched to reveal surface grain defects after directional solidification, hot isostatic pressurization, and solution heat treatment were all completed. These inspection reports were reviewed again for the bars which exhibited the defective grains, to check whether any other indications may be linked to their presence. Optical images of macro-etched bar 11570-1-9 shown in Figure 24(a) display small surface grains called freckles (Ref. 3) extended in a chain from the center to the outer radius at the bottom left end of the bar. Four other small freckles were noted near this angular location going along the bar's bottom surface to the right end. The specimen machining diagram in Figure 24(b) illustrates that specimens 019-LA2, 019-LB2, 019-LC1, and 019-LC2 which failed at grains were in approximate alignment with these surface freckles. Optical images of macro-etched bar 11570-2-2 are shown in Figure 25(a). Single small freckles are located at the center and outer radius at the bottom left end of the bar. Two elongated grain features called slivers were noted at this angular location going along the bar's bottom surface adjacent to the left end. The specimen machining diagram in Figure 25(b) illustrates that specimen 570-2-2-L2 roughly lines up with the freckle at the left end, while 570-2-2-L6 is not far from the sliver. Both of those specimens failed at defective grains. These observations suggested that small defective grains comparable to the surface freckles existed inside the volume of this bar, and that surface freckles could be considered indicators of such grains inside the bar.

However, this relationship was not always observed. Optical images of macro-etched bar 11471-1-7 shown in Figure 26(a) display small surface freckles extended in a chain from the center to the outer radius at the bottom left end of the bar. Several other small surface freckles were noted near this angular location at the bar's bottom surface adjacent to the left end. The specimen machining diagram in Figure 26(b) illustrates that specimen 117-LA1 which failed at an internal defective grain was at the opposite right end and angular location from these freckles. Freckles were apparently not always at the surface of bar locations containing internal defective grains. A more reliable non-destructive evaluation method would be preferable. Ultrasonic evaluations of grain size and grain uniformity have had success in some polycrystalline superalloys, and thus it may possible to adopt such methodology for detecting defective grains in single crystals (Ref. 21). Advancements of sensitivity and resolution have been reported in computerized x-ray tomography, that might also present opportunities for addressing this problem (Ref. 22).

(a)

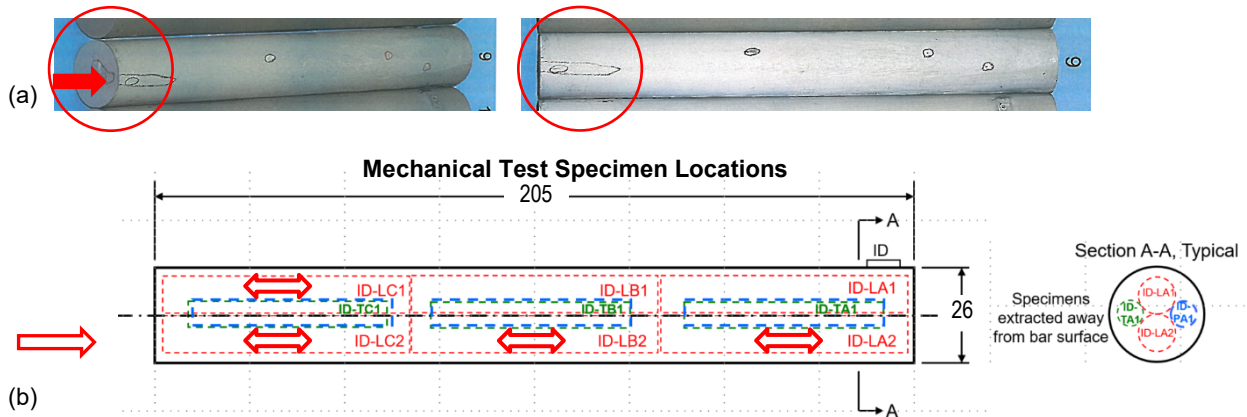**Mechanical Test Specimen Locations**

(b)

Figure 24.—Images of (a) macro-etched bar 11570-1-9 showing circled freckle grains, (b) specimen extraction diagram. The angular location of specimens 019-LA2, 019-LB2, 019-LC1, 019-LC2 lined up with freckle grains on the left end of the parent bar 11570-1-9.

(a)

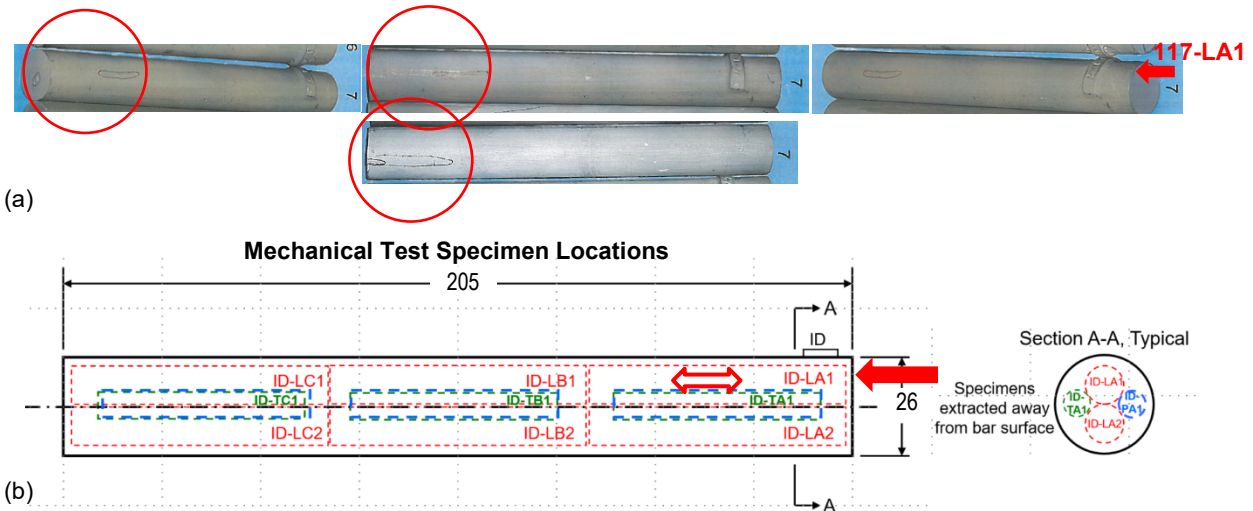**Mechanical Test Specimen Locations**

(b)

Figure 25.—Images of (a) macro-etched bar 11471-1-7 showing circled freckle grains, (b) specimen extraction diagram. The location of specimen 117-LA1 was not near freckle grains on the left end of the parent bar 11471-1-7.

(a)

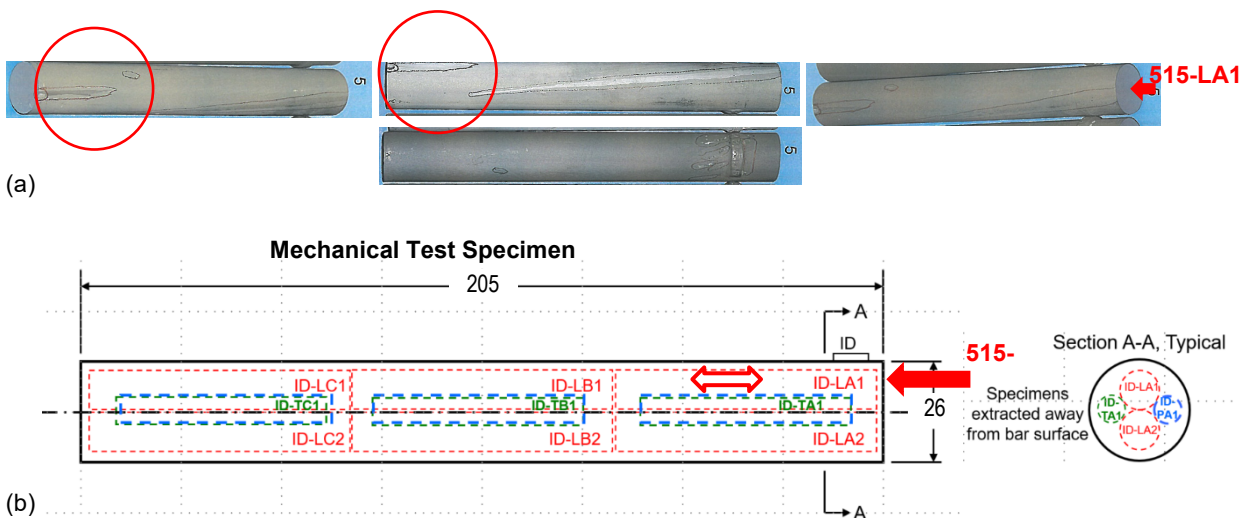**Mechanical Test Specimen**

(b)

Figure 26.—Images of (a) macro-etched bar 11435-1-5 showing circled freckle and high angle grains, (b) specimen extraction diagram. The location of specimen 515-LA1 was not near freckle grains on the left end of the parent bar 11435-1-5.

21

4.0   Summary and Conclusions

Fatigue tests were performed on single crystal superalloy specimens in the uncoated and coated forms, some exposed to prior oxidation plus hot corrosion and others not. Some of these specimens had surprisingly low fatigue lives, which were found to be directly related to the presence of defective grains. For these short LCF lives specimen failures initiated from defective grains which exhibited both somewhat modified composition and different orientation than the parent single crystal specimens. Their fatigue lives did not correlate with the presence of a coating or application of the exposures. Instead, total fatigue life significantly decreased and crack growth accounted for a larger fraction of life with increasing size of the defective grains. These specimens often, but not always, came from single crystal bars having small grains (freckles) aligned on nearby bar surfaces.

It can be concluded from this work that:

1) The presence of defective grains in these specimens can give significantly shortened fatigue lives, hence these defects have a significant impact on fatigue lives.

2) Increasing size of these undesirable grains tends to produce decreasing fatigue life, with crack propagation accounting for an increasing fraction of total fatigue life.

3) These defective grains can in some cases be in line with other grains ("freckles") intersecting the surface of a bar.

References

1. M. Gell, G.R. Leverant, "The Fatigue of the Nickel-base Superalloy, MAR-M200, in Single Crystal and Columnar-grained Forms at Room Temperature," *Trans. AIME*, V. 242, 1968, pp. 1869-1879.

2. F.L. VerSnyder, M.F. Shank, "The Development of Columnar Grain and Single Crystal High Temperature Materials Through Directional Solidification," *Mat. Sci. Eng.*, V. 6 (4), 1970, pp. 213-247.

3. D.H. Duhl, "Single Crystal Superalloys", in *Superalloys, Supercomposites, and Superceramics*, ed. by J.K. Tien, T. Caulfield, Academic Press, 1989, pp. 150-160.

4. S.D. Bond, J.W. Martin, "Surface Recrystallization in a Single Crystal Nickel-based Superalloy," *J. Mater Sci.*, V. 19, 1984, pp. 3867–3872.

5. S. Tin, T.M. Pollock, W.T. King, "Carbon Additions and Grain Defect Formation in High Refractory Nickel-base Single Crystal Superalloys," *Superalloys 2000*, Proc. of the Ninth International Conference on Superalloys, eds. T.M. Pollock, R.D. Kissinger, R.R. Bowman, K.A. Green, M. McLean, S. Olson, and J.J. Schirra, The Minerals, Metals & Materials Society, Warrendale, PA, 2000, pp. 201-210.

6. R. Burgel, P.D. Portella, J. Preuhs, "Recrystallization in Single Crystals of Nickel Base Superalloys," *Superalloys 2000*, Proc. of the Ninth International Conference on Superalloys, eds. T.M. Pollock, R.D. Kissinger, R.R. Bowman, K.A. Green, M. McLean, S. Olson, J.J. Schirra, The Minerals, Metals, & Materials Society, Warrendale, PA, 2000, pp. 229-238.

7. K. Harris, G.L. Erickson, S.L. Sikkenga, W.D. Brentnall, J.M. Aurrecoechea, K.G. Kubarych, "Development of the Rhenium Containing Superalloy CMSX-4 & CM 186 LC for Single Crystal Blade Applications in Advanced Turbine Engines," *Superalloys 1992*, Proc. of the Seventh International Conference on Superalloys, eds. S.D. Antolovich, R.W. Stusrud, R.A. MacKay, D.L. Anton, T. Khan, R.D. Kissinger, D.L. Klarstrom, The Minerals, Metals & Materials Society, Warrendale, PA, 1992, pp. 297-306.

8. D.C. Cox, B. Roebuck, C.M.F. Rae, R.C. Reed, "Recrystallisation of Single Crystal Superalloy CMSX-4," *Mat. Sci. Tech.*, V. 19 (4), 2003, pp. 440-446.

9. C. Zambaldi, F. Rotors, D. Raabe, U. Glatzel, "Modeling and Experiments on the Indentation Deformation and Recrystallization of a Single-crystal Nickel-base Superalloy," *Mat. Sci. Eng. A*, V. 454-455, 2007, pp. 433-330.

10. C. Panwisawas, H. Mather, J.-C. Gebelin, D. Putman, C.M.F. Rae, R.C. Reed, "Prediction of Recrystallization in Investment Cast Single-crystal Superalloys," *Acta Mat.*, V. 61, 2013, pp. 51-66.

11. J.R. Li, J.Q. Zhao, S.Z. Liu, M. Han, "Effects of Low Angle Boundaries on the Mechanical Properties of Single Crystal Superalloys DD6," S*uperalloys 2008*, Proc. of the Eleventh International Conference on Superalloys, eds. R.C. Reed, K.A. Green, P. Caron, T.P. Gabb, M.G. Fahrmann, E.S. Huron, S.A. Woodard, The Minerals, Metals, & Materials Society, Warrendale, PA, 2008, pp. 443-451.

12. C.-Y. Jo, H.-M. Kim, "Effect of Recrystallization on Microstructural Evolution and Mechanical Properties of Single Crystal Nickel Based Superalloy CMSX-2 Part 2 - Creep Behavior of Surface Recrystallized Single Crystal," *Mat. Sci. Tech.*, V. 19(12), 2003, pp. 1671-1676.

13. J. Menga, T. Jin, X. Suna, Z. Hua, "Effect of Surface Recrystallization on the Creep Rupture Properties of a Nickel-base Single Crystal Superalloy," *Mat. Sci. Eng. A*, V. 527, 2010, pp. 6119–6122.

14. J.J. Moverare, S. Johansson, R.C. Reed, "Deformation and Damage Mechanisms During Thermal–mechanical Fatigue of a Single-crystal Superalloy," *Acta Materialia*, V. 57, 2009, pp. 2266–2276.

15. J.A. Nesbitt, R.A. Miller, T.P. Gabb, S.L. Draper, I.E. Locci, C.K. Sudbrack, "LCF Life of NiCr-Y Coated Disk Alloys After Shot Peening, Oxidation and Hot Corrosion," NASA/TM—2020-220467, Washington, D.C., March 2020.

16. T.P. Gabb, J.A. Nesbitt, D. Haas, J. Telesman, S.L. Draper, B.J. Puleo, R.B. Rogers, R.A. Miller, "Fatigue Life of a NiCr-Coated Powder Metallurgy Disk Superalloy After Varied Processing and Exposures," NASA/TM—2018-220008, National Aeronautics and Space Administration, Washington, D.C., Nov. 2018.

17. NASGRO® 9.0, Fracture Mechanics & Fatigue Crack Growth Software, 2018.

18. R.A. MacKay, T.P. Gabb, J.L. Smialek, M.V. Nathal, "A New Approach of Designing Superalloys for Low Density," *J. of Metals*, V. 62, 2010, pp. 48–54.

19. S. Suresh, G.F. Zamiski and R.O. Ritchie, "Oxide-Induced Crack Closure: An Explanation for Near-Threshold Corrosion Fatigue Crack Growth Behavior," *Met. Trans. A*, V. 12A, August 1981, pp. 1435-1443.

20. J.C. Newman Jr., "The Merging of Fatigue and Fracture Mechanics Concepts: a Historical Perspective," *Progress in Aerospace Sciences*, V. 34, 1998, pp 347-390.

21. P.D. Panetta, L.G. Bland, M. Tracy, W. Hassan, "Ultrasonic Backscattering Measurements of Grain Size in Metal Alloys," *TMS 2014: 143rd Annual Meeting & Exhibition Supplemental Proceedings*, ed. by The Minerals, Metals & Materials Society, Springer, Warrendale, PA, 2014, pp. 723-730.

22. A. du Plessis, I. Yadroitsev, I. Yadroitsava, S.G. Le Roux, "X-Ray Microcomputed Tomography in Additive Manufacturing: A Review of the Current Technology and Applications," 3D Printing and Additive Manufacturing, V. 5 (3), 2018, pp. 227-247.